Thermal Cracking in Westerly Granite Monitored Using Direct Wave Velocity, Coda Wave Interferometry, and Acoustic Emissions

Luke Griffiths, Olivier Lengliné, Michael J Heap, Patrick Baud, Jean Schmittbuhl

AGU PUBLICATIONS

JGR

Journal of Geophysical Research: Solid Earth

RESEARCH ARTICLE
10.1002/2017JB015191

Key Points:
- We performed heating and cooling cycles of Westerly Granite to a maximum temperature of 450°C at ambient pressure
- We monitored acoustic emissions and changes in velocity with temperature using direct traveltime and coda wave interferometry techniques
- We quantified both the reversible and irreversible effects of thermal expansion of crystals on ultrasonic velocity

Supporting Information:
- Supporting Information S1

Correspondence to:
L. Griffiths,
luke.griffiths@unistra.fr

Citation:
Griffiths, L., Lengliné, O., Heap, M. J., Baud, P., & Schmittbuhl, J. (2018). Thermal cracking in Westerly Granite monitored using direct wave velocity, coda wave interferometry, and acoustic emissions. *Journal of Geophysical Research: Solid Earth*, *123*, 2246–2261. https://doi.org/10.1002/2017JB015191

Received 2 NOV 2017
Accepted 23 FEB 2018
Accepted article online 1 MAR 2018
Published online 23 MAR 2018

Thermal Cracking in Westerly Granite Monitored Using Direct Wave Velocity, Coda Wave Interferometry, and Acoustic Emissions

L. Griffiths[1], O. Lengliné[1], M. J. Heap[1], P. Baud[1], and J. Schmittbuhl[1]

[1]Institut de Physique de Globe de Strasbourg, Université de Strasbourg/EOST, CNRS UMR 7516, Strasbourg, France

Abstract To monitor both the permanent (thermal microcracking) and the nonpermanent (thermo-elastic) effects of temperature on Westerly Granite, we combine acoustic emission monitoring and ultrasonic velocity measurements at ambient pressure during three heating and cooling cycles to a maximum temperature of 450°C. For the velocity measurements we use both *P* wave direct traveltime and coda wave interferometry techniques, the latter being more sensitive to changes in *S* wave velocity. During the first cycle, we observe a high acoustic emission rate and large—and mostly permanent—apparent reductions in velocity with temperature (*P* wave velocity is reduced by 50% of the initial value at 450°C, and 40% upon cooling). Our measurements are indicative of extensive thermal microcracking during the first cycle, predominantly during the heating phase. During the second cycle we observe further—but reduced—microcracking, and less still during the third cycle, where the apparent decrease in velocity with temperature is near reversible (at 450°C, the *P* wave velocity is decreased by roughly 10% of the initial velocity). Our results, relevant for thermally dynamic environments such as geothermal reservoirs, highlight the value of performing measurements of rock properties under in situ temperature conditions.

1. Introduction

The influence of temperature on the physical and mechanical properties of rock is of interest to many areas of Earth science and engineering, and at a wide range of scales. In granite, the thermal expansion of minerals results in the build-up of thermal stresses during heating and may lead to thermal microcracking (Kranz, 1983). Thermal microcracking has been shown to increase porosity (Chaki et al., 2008; C. David et al., 1999; Nasseri et al., 2007; Reuschlé et al., 2003; X.-Q. Wang et al., 2013), increase permeability (Chaki et al., 2008; Glover et al., 1995; Jones et al., 1997; Meredith et al., 2012; X.-Q. Wang et al., 2013), and reduce uniaxial strength (Nasseri et al., 2007) and stiffness (E. C. David et al., 2012; Walsh, 1965).

Fredrich and Wong (1986), for example, studied the micromechanics of thermal cracking in three crustal rocks, including Westerly Granite, in which—through microscopic observation of a suite of thermally stressed samples—they found that thermal microcracking occurs from temperatures within the range of 100–165°C and found that all crystal boundaries were cracked in the granite heated to 500°C. Using a 2-D square inclusion model, they link these threshold temperatures for thermal microcracking to the thermal expansion mismatch between the inclusion and the surrounding material. In another study of thermal microcracking in granite, Thirumalai and Demou (1973) measured the thermal dilation of two granites (Halecrest and Charcoal) during cyclical heating and cooling. They observed a permanent dilation of the granites following the first cycle, due to an increase in thermal microcrack porosity. However, they found the magnitude of microcracking with subsequent cycles to be much diminished, with no permanent dilation following the third heating/cooling cycle.

In the laboratory, a common technique to detect microcracking is acoustic emission (AE) monitoring. AE are transient elastic waves produced during microcrack extension, and AE monitoring has been applied to thermal microcracking in granite (Chen et al., 2017; Glover et al., 1995; Jones et al., 1997; Siratovich et al., 2015; Todd, 1973). For example, Glover et al. (1995) heated La Peyratte granite at 1°C/min to 900°C while monitoring AE and observed an onset of AE at around 80°C, and a spike in the AE rate at 573°C. Around 573°C corresponds to the temperature of the alpha/beta transition of quartz at room pressure, which is accompanied by a marked thermal expansion, thus increasing thermal stresses and leading to further thermal microcracking. Todd (1973) also used AE monitoring to study the influence of multiple heating and cooling cycles (to a maximum temperature of 300°C) on Westerly Granite. Todd (1973) observed AE mostly as

the unheated rock was heated for the first time; very few AE were observed during cooling or during repeated thermal stressing cycles. Another example of AE monitoring during cooling (which we note are rare in the literature) is a study by Browning et al. (2016), who monitored thermal microcracking in volcanic rocks (a basalt and a dacite). Browning et al. (2016) found the vast majority of AE to occur during cooling, which they attribute to thermal microcracking, underlining the merit for further study of AE monitoring during cooling.

The *P* (pressure) wave and *S* (shear) wave ultrasonic velocities of rock (herein v_P and v_S, respectively) are particularly sensitive to microcracking and have been shown to permanently decrease when the build-up of thermal stresses leads to thermal microcracking (Chaki et al., 2008; C. David et al., 1999; Johnson et al., 1978; Jones et al., 1997; Nasseri et al., 2007). C. David et al. (1999) found the v_P of La Peyratte granite to decrease from roughly 5.5 to 3.7 km/s when heated to 450°C and cooled back to room temperature. The same thermal stressing procedure was applied by Nasseri et al. (2007) to Westerly Granite, following which they observed a decrease in v_P from roughly 4.5 to 3.0 km/s. There is, however, a lack of direct wave velocity measurements performed above room temperature in the literature. Examples include Zappone and Benson (2013), who measured v_P and v_S of a metapelite from the southern Alps in northern Italy during heating to 750°C under high confining pressures of 200, 300, and 400 MPa, revealing the temperature of the quartz α/β transition. To examine the influence of temperature on the matrix velocity of rock, Kern (1982) measured v_P and v_S of samples of various rocks under a high confining pressure of 600 MPa and temperatures of up to 600°C. Confining pressure was applied with the aim of closing all microcracks, and the wave velocities were seen to decrease with increasing temperature. H. F. Wang et al. (1989) measured v_P of Westerly Granite during heating to 300°C and cooling under confining pressures of 7, 28, and 55 MPa, finding v_P to decrease with increasing temperature, from ~4.5 km/s at room temperature to ~3.4 km/s at 300°C. H. F. Wang et al. (1989) found that for all confining pressures v_P decreased during heating and increased during cooling, returning to the velocity of the unheated rock.

Grêt et al. (2006) used another method, coda wave interferometry (CWI), to measure the influence of temperature on the wave velocity of Elberton Granite when heated to 90°C. CWI is a technique to infer small changes in wave velocity from assessments of small relative delays in multiply scattered waves using high-resolution cross correlations of waveforms (Snieder, 2002, 2006). Grêt et al. (2006) observed increasing time delays during heating, corresponding to an apparent decrease in wave velocity. Between 70 and 90°C they observed a strong nonlinear decrease in the apparent velocity with temperature, a result of thermal microcracking. During a second heating and cooling cycle, they observed a reversible thermo-elastic response of the waveforms to temperature. CWI, however, has yet to be used to monitor changes in rock microstructure resulting from thermal microcracking when heated to and cooled from higher temperatures.

Here we use a new approach, combining AE monitoring, measurements of v_P, and CWI to monitor microstructural changes in Westerly Granite during three heating and cooling cycles to a maximum temperature of 450°C. Through repeated heating and cooling cycles, we quantify the influence of the irreversible (thermal microcracking) and reversible (thermo-elastic deformation) changes in microstructure on the velocity of granite.

2. Materials and Methods

2.1. Materials

We selected Westerly Granite (from Rhode Island, USA) for this study as its physical and mechanical properties are well known, near isotropic (Lockner, 1998), and have been shown to exhibit permanent changes—through thermal microcracking—when heated (Nasseri et al., 2007; Nasseri, Schubnel, et al., 2009; H. F. Wang et al., 1989; Yong & Wang, 1980). Westerly Granite has a mineralogical composition in volumetric fraction of 27% quartz, 36% microcline, 30% plagioclase, 6% phyllosilicates, and 1% others, and a mean crystal size of 0.75 mm (Meredith & Atkinson, 1985). We show a backscattered scanning electron microscope (SEM) micrograph of a thin section of Westerly Granite in Figure 1. Labeled are grains of quartz (Qtz), microcline (Mc), plagioclase (Pl), and phyllosilicate (here biotite, Bt).

We cored three cylindrical samples of Westerly Granite in the same orientation and precision-ground their end-faces flat and parallel (diameter of 20 mm and a nominal length of 40 mm). Samples were oven-dried

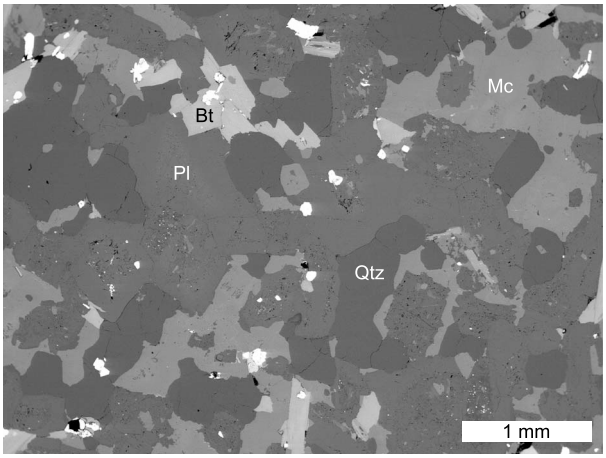

Figure 1. Backscattered scanning electron microscope micrograph of unheated Westerly Granite. Labeled are grains of quartz (Qtz), microcline (Mc), plagioclase (Pl), and phyllosilicate (here biotite, Bt).

at 40°C in-vacuo for at least 48 hr prior to experimentation. We assume that the granite block is sufficiently homogeneous and isotropic (Lockner, 1998) and that the influence of thermal stressing is sufficiently repeatable to compare measurements on different samples cored from the same block.

2.2. Experimental Procedure

2.2.1. Experimental Setup

The experimental setup (Figure 2)—designed specifically for acoustic measurements at high temperature—consists of a LoadTrac II servo-controlled uniaxial press, in which a rock sample is held between two vertical pistons made from heat resistant stainless steel (grade 310). A GSL-1100X tube furnace (MTI Corporation), which has a constant temperature zone of 80 mm in length, surrounds the sample. A custom-built air-cooling system is attached around the top of the upper piston to avoid exposing the AE transducer embedded within the upper piston and the load cell to potentially-damaging high temperature.

2.2.2. Thermal Load

In each experiment, a sample is subject to three heating and cooling cycles, at rate of 1°C/min, with a dwell time of 2 hr at the maximum temperature of 450°C. The maximum temperature is limited by the operating range of the acoustic transducers within the furnace (Figure 1). We performed in situ measurements of *P* wave traveltime and CWI on the first Westerly Granite sample, and for a second sample we monitored AE. During both experiments, the furnace temperature was recorded at 10 mm from the sample surface. During the first experiment (the velocity measurements), we also recorded the temperature at the center of the sample using a thermocouple (of diameter 1.5 mm) inserted through a 1.7 mm hole drilled radially, halfway along the sample length. A third granite sample was subject to the same thermal stress cycling procedure, and we performed "static" measurements of v_P and v_S at room temperature using a separate dedicated device before and after each cycle, for comparison with our in situ measurements.

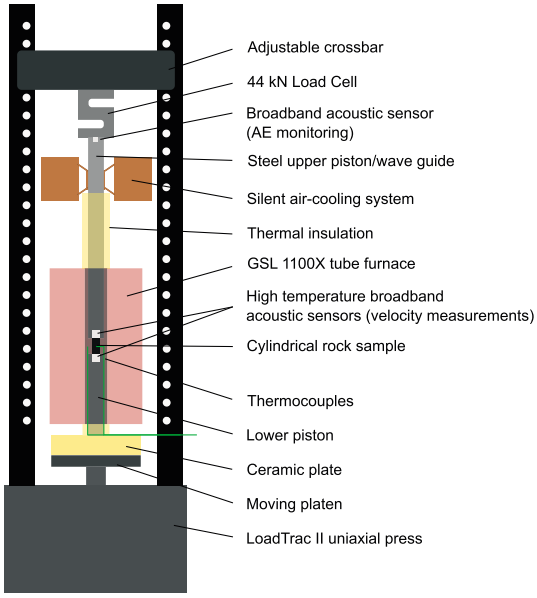

Figure 2. Schematic of the experimental setup for acoustic emission monitoring and velocity measurements. The setup consists of a LoadTrac II uniaxial press and a GSL 1100X tube furnace. For AE monitoring, a single acoustic sensor is embedded within the top of the upper piston. For CWI and *P* wave traveltime measurements, a pair of high-temperature sensors are in direct contact with opposing ends of the sample.

2.3. Measurements

2.3.1. *P* wave Velocity

For the in situ v_P measurements we used two acoustic sensors, a source and receiver, housed within each piston (Figure 2). The sensors were in direct contact with opposing faces of the granite sample and coupling was ensured, and kept constant by, a servo-controlled axial force of 100 N (~0.3 MPa) on the sample (coupling otherwise oscillates dramatically as the pistons thermally expand and contract). The sensors were S9215 high-temperature sensors from Physical Acoustics, which have a resonant frequency of 100 kHz (52 dB) and an operating frequency range of 80–560 kHz. During the three heating and cooling cycles, a signal generator connected to the upper transducer emitted a 200 kHz sinusoidal pulse every 50 ms and simultaneously triggered a National Instruments BNC 2110 acquisition card to record the preamplified (+40 dB preamplifier with a flat response above 2 kHz) voltage across the receiving transducer. Each recorded waveform was 2 ms in duration: 4,000 samples at a sampling rate of 2 MHz, including a pre-trigger recording time of 0.05 ms. The acquisition was repeated 50 times in succession, and the 50 recorded waveforms were stacked to increase the signal-to-noise ratio. We set a waiting time of 10 s between stacks, and acquisition continued throughout the three heating and cooling cycles.

To calculate the shift in *P* wave arrival time, we spliced the first 30 μs of the recorded waveforms and calculated the cross-correlation functions (in the frequency domain) between pairs of waveforms throughout the

experiment. Next, in the time domain, we performed a piecewise quadratic interpolation of each cross-correlation function around its maximum, and we calculated the time shift at the maximum of the newly interpolated cross-correlation function. We calculated the cumulative shift in *P* wave arrival time with experiment time to obtain the time shift with respect to the initial waveform.

At room temperature, and on a separate, dedicated, and calibrated setup, we made static measurements of v_P and v_S at ambient pressure and temperature, both before and following heating and cooling. We used two pairs of piezo-transducers in contact with opposing faces of the sample (each pair oriented either parallel or perpendicular to the sample length for *P* wave and *S* wave, respectively), with one emitting an ultrasonic wave (excited by a sinusoidal pulse: 700 kHz for *P* wave and multiple frequencies within the range of 100–500 kHz for *S* wave), and the other receiving. The velocities were calculated from the direct wave arrival times observed on an oscilloscope. Using the static v_P measurement of the unheated granite prior to heating and the shift in *P* wave arrival time measured during heating and cooling, we calculated v_P during the entire experiment.

2.3.2. Coda Wave Interferometry (CWI)

CWI considers an ultrasonic wave that becomes scattered and reflected multiple times by the boundaries of, or the heterogeneities within a medium (Snieder et al., 2002). The resulting waveform at a given location is the contribution of many scattered waves that have traveled along different raypaths. Following changes in the medium—which include velocity changes, the displacement of scatterers due to thermal or mechanical deformation, and the development of new scatterers—the traveltime of these scattered waves becomes delayed (Snieder, 2006). In the case of a velocity perturbation, Snieder (2002) showed that the shift in traveltime of the wave is proportional to the time traveled (equation (1)) and therefore may be significantly greater than the delay we observe in the direct arrivals.

$$\frac{\delta v}{v} = -\frac{\delta t}{t} \tag{1}$$

The scattered waves arrive later or earlier following a change in velocity, and the resulting waveform becomes elongated (apparent decrease in velocity) or compressed (apparent increase in velocity) in time. For a given velocity change, the ratio between time shift and traveltime is constant (equation (1)): the stretching of the waveform increases with increasing traveltime as later arrivals have traveled for longer at the new velocity.

There are two main methods used in CWI to calculate the relative time shift between waveforms. The first—and original—method involves calculating the cross-correlation function between the two waveforms in windows centered at different traveltimes (Poupinet et al., 1984; Snieder et al., 2002). The lag of the maximum of each cross-correlation function provides the time shift for a given traveltime, and their linear regression yields the relative time shift, $\frac{\delta t}{t}$. However, a potential problem with this method is that it approximates the time shift as a constant within each window (Larose & Hall, 2009).

The second approach for calculating $\frac{\delta t}{t}$—and the method used herein—is the stretching method, whereby we apply an array of relative time shifts to the first waveform and we select the value of $\frac{\delta t}{t}$ for which the stretched first waveform correlates most with the second (Larose & Hall, 2009; Sens-Schönfelder & Wegler, 2006). Following Larose & Hall (2009), we use a spline interpolation in the time domain to stretch each waveform, noted h_k, onto a series of new time vectors $t(1 - a)$, where a is a value of the relative time shift, $\frac{\delta t}{t}$. We then calculate the cross-correlation function (in the frequency domain), between a reference waveform h_0 and the shifted waveform $h_k[t(1 - a)]$, and the relative time shift is equal to the value of a for which the peak of the cross-correlation function is maximal, noted $a_{k,\,0}$ (T is the length in time of the waveforms, here 0.5 ms).

In our experiments, the correlation between the reference waveform, h_0, and subsequent waveforms, h_k, deteriorates with temperature due to the strong perturbation of the medium. To counter this, we calculate instead the relative time shift $a_{k,\,k\,-\,1}$ between consecutive waveforms h_k and $h_{k\,-\,1}$. In this case, a scaling factor is required to infer the relative time shift with respect to the reference waveform, $a_{k,\,0}$ (equation (2)). The scaling factor is a function of the previous relative time shifts $a_{i,\,i\,-\,1}$.

$$a_{k,0} = \Pi_{i=1}^{k}\left(a_{i,i-1} + 1\right) - 1 \tag{2}$$

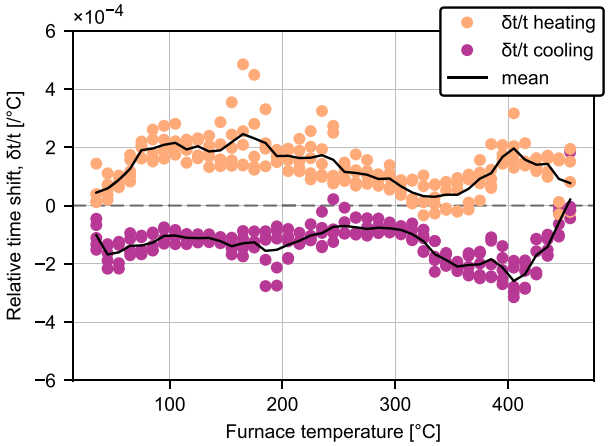

Figure 3. The CWI relative time shift per °C with temperature (averaged over intervals of 10°C) calculated from waveforms recorded over five cycles of heating and cooling of a fused quartz sample. The black solid line represents the mean relative time shift with temperature with which we calibrated CWI measurements made on the Westerly Granite sample.

With our limited sampling of the wavefield, we cannot clearly identify the wave path, which mostly contribute to the coda. Here as the wavelength is of the same order of magnitude as the sample dimensions, we expect that the coda is dominated by surface waves traveling around the cylindrical sample (as concluded by Grêt et al., 2006, under similar experimental conditions). It is also possible that multiple-reflected waves contribute to the coda, as the pulse wavelength is slightly less than the sample dimensions.

2.3.3. Calibration of the Acoustic Sensors

It is important to account for apparent time shifts due to external biases of the experimental procedure, including whether the response of the acoustic sensors is sensitive to temperature. Zhang et al. (2013) applied CWI to the mechanical deformation of concrete and, to quantify the influence of fluctuations in ambient temperature on the relative time shift, they simultaneously performed CWI on a second, un-stressed concrete sample. Zhang et al. (2013) calculated the relative time shift from the two experiments to isolate the influence of mechanical deformation on $\frac{\delta t}{t}$.

Here we performed both CWI and v_P measurements on a sample of fused quartz (with the same dimensions as the granite samples). We expected to see a low time shift in both the direct *P* wave and CWI measurements due to the low changes in v_P and v_S with temperature (measured to increase by ~2% and ~3%, respectively, when heated to 450°C; Fukuhara and Sanpei, 1994), and because of the low thermal expansion coefficient of fused quartz. Regarding the influence of thermal expansion, if we assume that the relative time delay is equal to the relative elongation of raypaths, which is in turn equal to the linear thermal expansion coefficient of fused quartz, we find a low $\frac{\delta t}{t}$ of 5.4×10^{-7}/°C. Any deviation from these relative time shifts is expected to originate from external factors, including the sensor response, which must be corrected for when measurements are made using the same experimental apparatus on rock samples of the same geometry.

We observed an increase in v_P of the fused quartz sample by around 2.7% at 450°C (similar to the ~3% increase measured by Fukuhara and Sanpei, 1994). However, we measured a positive relative time shift using CWI (~1.5×10^{-4}/°C; Figure 3), indicating an apparent decrease in the CWI wave velocity with temperature (equation (1)) significantly greater than that due to the linear thermal expansion coefficient of quartz. We expect that the observed relative time shift (Figure 3) may be due to wave scattering/reflection within the steel casings of the sensors, and sensitivity of the electro-elastic response of the piezo-ceramic transducers to temperature. The signal we measured for the fused quartz sample contains all these possible influences, which we correct for in the measurements made on the granite sample. Note that we expect the hysteresis of the relative time shift with respect to furnace temperature (Figure 3) to be due to the temperature of the acoustic sensors, which is lower during heating and higher during cooling.

Figure 4 shows the Westerly Granite sample temperature with time (Figure 4a) and the amplitudes in grey-scale of the first 0.5 ms of the recorded waveforms (Figure 4b), which we used for both CWI and v_P measurements. In Figure 4c, we show the same waveforms but stretched by applying the mean relative time shift with temperature measured on the sample of fused quartz (Figure 3), to illustrate the relative time shift correction.

2.3.4. Acoustic Emission (AE) Monitoring

For AE monitoring, a single broadband AE sensor is housed facing toward the sample within the center of the upper piston (Figure 2) to best capture the AE energy. To test this configuration, we simultaneously recorded the AE produced by a Hsu-Nielsen lead break source—a 0.5 mm diameter 2H pencil lead of approximately 3 mm in length broken by pressing it against the surface of the granite sample—using two identical sensors, one within the piston (as in Figure 2) and one adjacent, attached to the outside of the piston (details of the AE acquisition are described in the paragraph below). We observed a greater amplitude and improved frequency content using the AE sensor embedded within the piston. The piston, acting as a continuous waveguide (thus avoiding problems associated with attenuation at surface interfaces), applied a servo-controlled load of 100 N (~0.3 MPa) on the sample to ensure a constant coupling between the sensor and the sample.

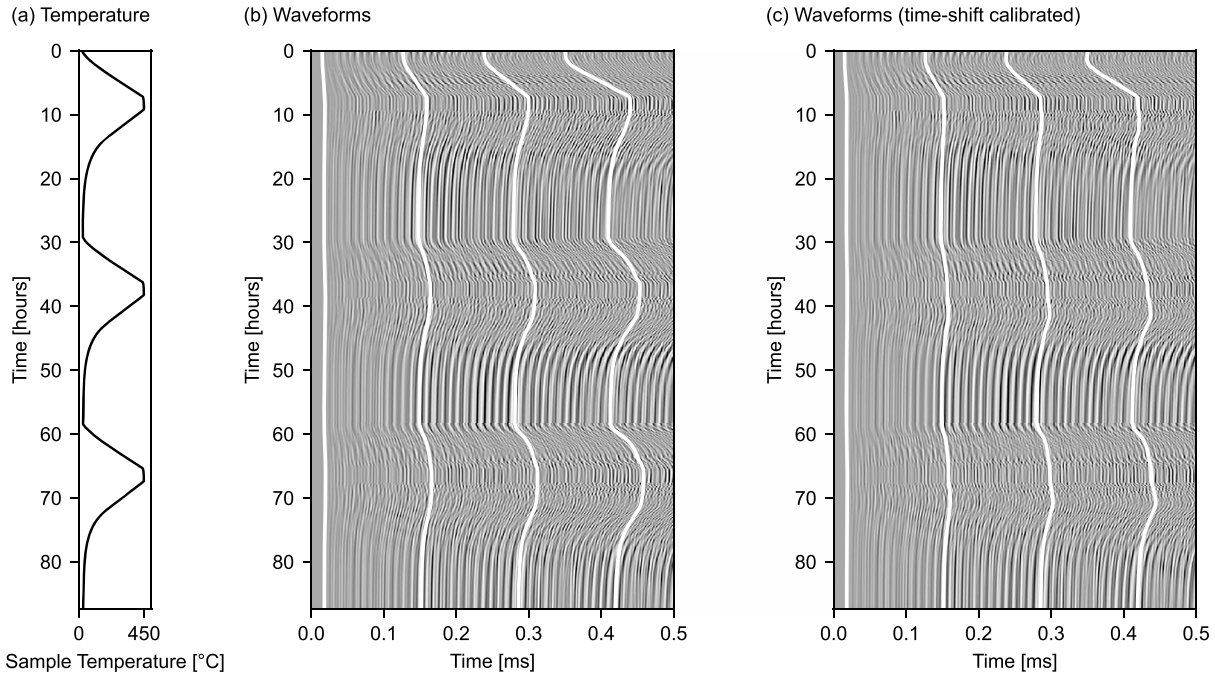

Figure 4. CWI during three heating and cooling cycles. (a) Westerly Granite sample temperature against experiment time. (b) The first 0.5 ms of the original recorded waveforms with experiment time. (c) The first 0.5 ms of the stacked waveforms with experiment time shifted by the relative time shift measured on the sample of fused quartz. A waiting time of 10 s was set between stacks. The white lines illustrate the stretching of the waveform with time, by applying the noncalibrated and calibrated cumulative time shifts measured with CWI to four distinct initial arrival times.

Without the servo-controlled load, the coupling oscillates dramatically as the pistons deform with temperature, ultimately influencing the AE detection threshold.

The AE sensor was a micro80 miniature sensor from Physical Acoustics, which has a bandwidth of 200–900 kHz and a resonant frequency of 325 kHz. The sensor was connected to a 1283 USB AE Node: a single-channel AE digital signal processor with a built-in 26 dB preamplifier and integrated analogue low- and high-pass filters (set to 20 kHz and 1 MHz, respectively). When the preamplified voltage across the transducer crossed the 40 dB detection threshold (with respect to a 1 μV reference voltage), an AE "hit" was registered, and the system then counted the subsequent number of oscillations across the voltage threshold (also known as ring-down counts). The AE trigger system parameters were set to 400 μs peak definition time (the time following detection within which the peak voltage—and therefore the AE amplitude—may be determined), 400 μs hit definition time (the maximum time between consecutive threshold crossings, above which they are considered as part of separate hits), and a 1,000 μs hit lockout time (the minimum time between consecutive hits). These parameters were selected to correctly capture the AE produced by a Hsu-Nielson source (lead break) on the surface of the granite sample, which produces an AE hit of amplitude 79 dB. When triggered, the 1283 USB AE Node also recorded the first 7 ms of each AE waveform (7,000 time samples at 1 MHz sampling rate) with a 100 μs pretrigger. Studying the waveforms, we postprocessed the AE data to remove any hits resembling electrical spikes, which corresponded to all hits that had both an amplitude greater than 55 dB and a number of ring-down counts lower than 60. For comparison, genuine AE hits of more than 55 dB in amplitude had a mean number of ring-down counts of 460. The number of discounted hits corresponded to 105 out of 596, 45 out of 137, and 43 out of 89 AE hits over the course of the first, second, and third cycles, respectively.

3. Results

3.1. *P* wave Velocity

Table 1 shows the measurements of v_P and v_S made at room temperature on a thermally stressed Westerly Granite sample using a separate dedicated setup. Before heating, v_P was 4.89 km/s, decreasing to

Table 1
P Wave and S Wave Velocities, Measured Before and Following the Heating/Cooling Cycles to 450°C, and Number of Detected AE Hits During Heating and Cooling of Each Cycle

	v_P (km/s)	v_S (km/s)	AE hits during heating	AE hits during cooling
Un-heated	4.89	2.7	-	-
Heated to 450°C	2.95	-	224	267
2× heated to 450°C	2.77	-	19	73
3× heated to 450°C	2.71	2.2	22	24

2.95 km/s following the first heating and cooling cycle. We measure smaller decreases, from 2.95 to 2.77 km/s, and finally to 2.71 km/s following the second and third cycles, respectively (Table 1). We measure a decrease in v_S from 2.7 km/s before heating to 2.2 km/s following the third cycle (Table 1).

Figure 5a shows the in situ measurements of v_P against sample temperature during each heating and cooling cycles. The initial value of v_P ("v_P preheat" in Figure 5a) is the value measured using a separate calibrated device at room temperature prior to heating (4.97 km/s), which is then recalculated taking in to account the measured traveltime shift during heating and cooling. As the sample is first heated to 50°C, v_P initially shows a slight increase (Figure 5a). Between 100 and 450°C v_P shows a continuous decrease to 2.50 km/s at 450°C. During cooling, v_P recovers to 3.01 km/s, resulting in a permanent net decrease of 1.96 km/s over the first cycle. A similar permanent decrease in v_P following a single heating/cooling cycle is also observed in our room temperature measurements on another thermally stressed sample of Westerly Granite (Table 1) and in the literature: (Nasseri et al., 2007) measured at room temperature a similar decrease in v_P of Westerly Granite when heated to 450°C from 4.5 to 3.0 km/s. Agreement with these standard room temperature measurements adds veracity to our in situ measurement method.

During the second cycle, the in situ v_P decreases from 3.01 to 2.44 km/s at 450°C and increases back to 2.90 km/s upon cooling (0.11 km/s net decrease; Figure 5a). Finally, during the third cycle, v_P decreases to 2.42 km/s at 450°C, returning to 2.85 km/s upon cooling (0.05 km/s net decrease; Figure 5a). The v_P of the sample was remeasured using a separate device following all cycles (black circle in Figure 5a), which is the same as the final value of v_P calculated from the cumulative time shift.

3.2. Coda Wave Interferometry

We calculated the relative time shift between the first 0.5 ms of consecutive waveforms (Figure 4b) using the stretching method (Larose & Hall, 2009; Sens-Schönfelder & Wegler, 2006) as described previously, before correcting for the relative time shift measured on the fused quartz sample (Figure 3). The calibrated and noncalibrated cumulative CWI time shifts for all three cycles are shown in Figure S1 of the supporting information. In Figures 4b and 4c, the white solid lines illustrate the stretching of the waveform during heating and cooling by applying the noncalibrated and calibrated CWI time shifts, respectively, to four distinct initial arrival times. We see that these lines follow the shift in the peaks and troughs of the waveforms. Overall, we observe an elongation of the waveforms during heating and a compression during cooling—a positive and negative relative time shift respectively—corresponding to an apparent decrease in velocity with increasing temperature (equation (1)).

Figure 5b shows the calibrated relative time shift per °C, $\frac{\delta t}{t}$, averaged over a 10°C increase/decrease in sample temperature during each cycle. As the rock is heated for the first time, the relative time shift is initially negative (Figure 5b), corresponding to an apparent increase in velocity with temperature up until 60°C. Between 60 and 150°C the relative time shift is positive and increases linearly with sample temperature. Above 150°C, the time shift is constant with temperature, remaining roughly between 5×10^{-4}/°C and 7.5×10^{-4}/°C. Measurements of relative time shift are greater in amplitude than those measured on the sample fused quartz sample (~1.5×10^{-4}/°C; Figure 3). During cooling, $\frac{\delta t}{t}$ remains positive between 440 and 400°C, before becoming negative and showing a linear decrease as the sample cools (an apparent increase in velocity). The amplitude of the relative time shift during cooling remains below 4×10^{-4}/°C, lower than during heating. Overall, we find similar values to those of Grêt et al. (2006)— $\frac{\delta t}{t}$ of between 2×10^{-4}/°C and 6×10^{-4}/°C—when they heated and cooled Elberton Granite to a maximum temperature of 90°C, confirming our approach.

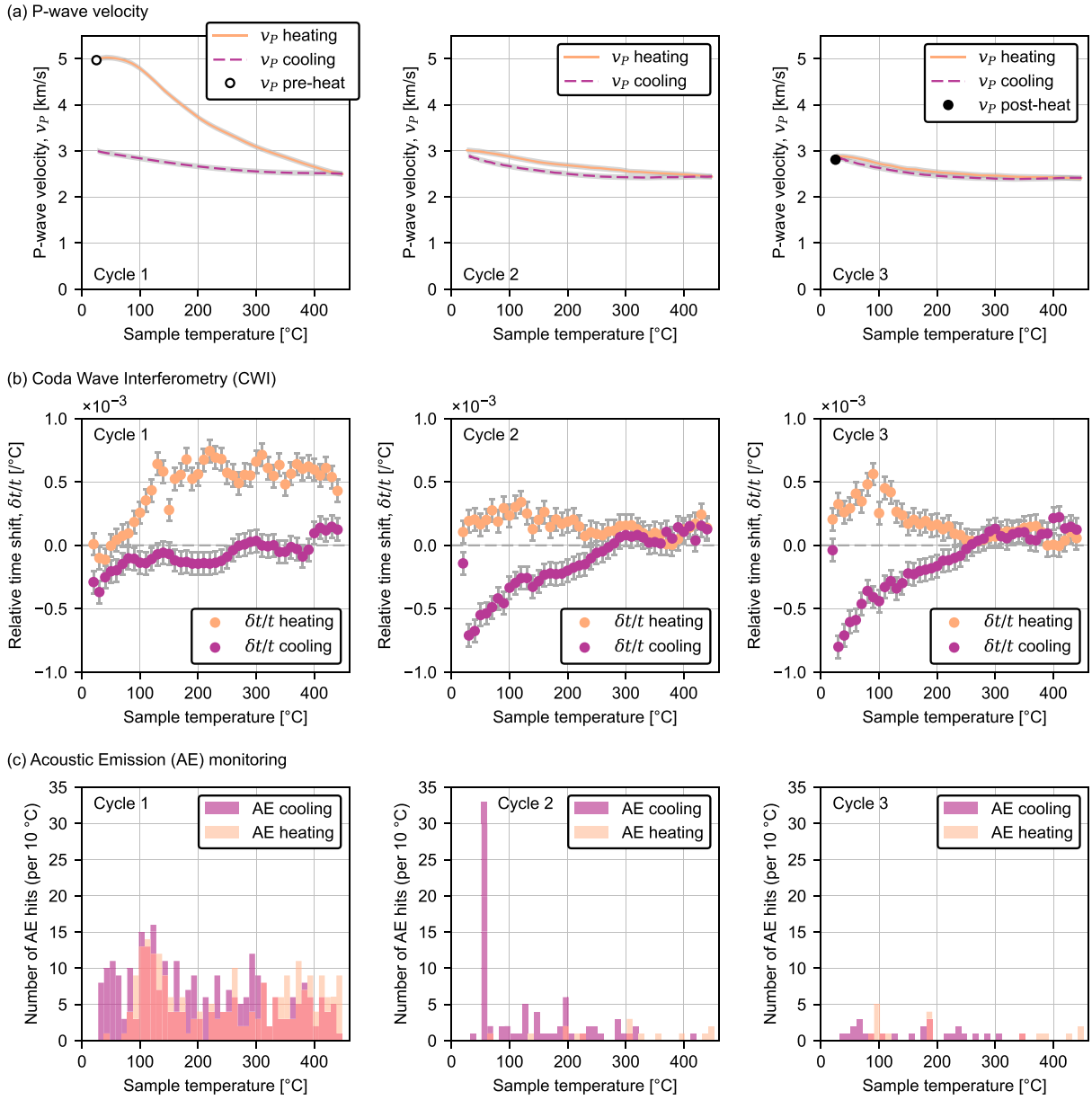

Figure 5. Measurements made during three heating/cooling cycles of Westerly Granite to a maximum temperature of 450°C. (a) *P* wave velocity: the circles represent v_P measurements made at room temperature before (open) and after heating (filled). The lines represent v_P against sample temperature during heating (solid) and cooling (dashed), calculated from the cumulative shift in *P* wave arrival time with temperature and the initial v_P of the unheated rock, measured prior to heating (4.97 km/s). Error (shaded grey) is equal to the precision of the initial v_P measurement. (b) CWI: the relative time shift per °C (averaged over 10°C intervals) against sample temperature. The error bars represent the potential variability, equal to two standard deviations from the mean of the relative time shifts measured on the fused quartz sample (Figure 3). (c) AE monitoring: the bars show the number of AE hits in bins of 10°C against sample temperature during heating and cooling.

In the following cycles the relative time shift is initially positive during heating (apparent decrease in velocity), at around 2×10^{-4}/°C throughout cycle 2 and 3.5×10^{-4}/°C during cycle 3 (Figure 5b). The time shift decreases with temperature, remaining lower than during the first cycle between 150 and 450°C. During the cooling phase of cycles 2 and 3, the relative time shifts are very similar. Initially close to zero, $\frac{\delta t}{t}$ increases to around 2.5×10^{-4}/°C at 420°C and then decreases during the rest of each cooling phase, becoming negative at around 300°C. This corresponds to an acceleration of the apparent wave velocity as the granite cools.

Regarding the influence of deformation on traveltime, we can apply the same calculation as for the fused quartz, equating the relative time shift due to the relative elongation of raypaths to the linear thermal

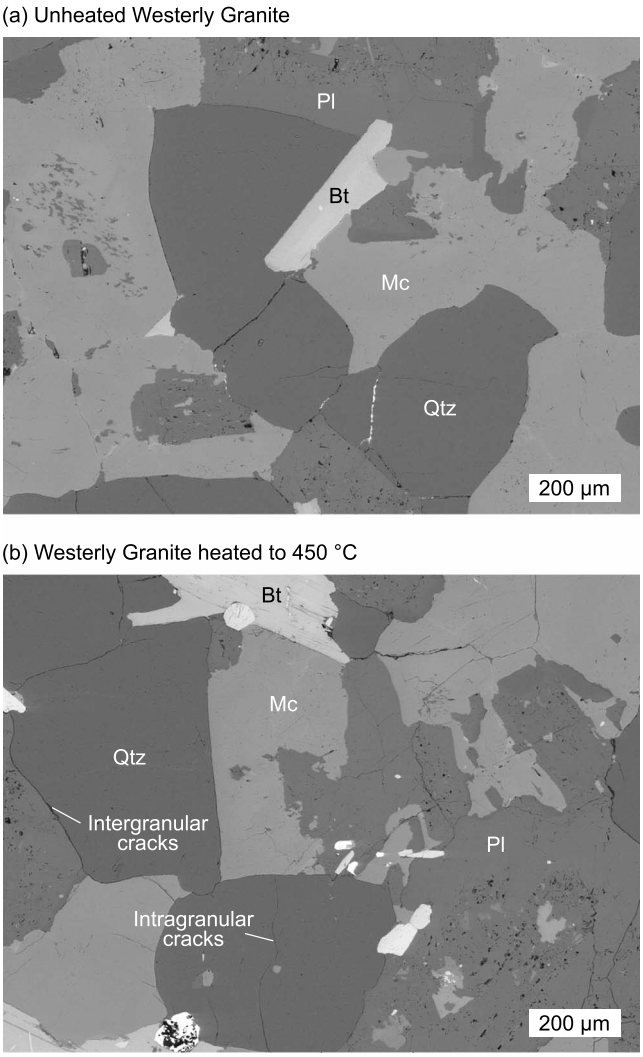

Figure 6. Backscattered scanning electron microscope micrographs of samples of Westerly Granite both (a) unheated and (b) heated to 450°C and cooled. Labeled are grains of quartz (Qtz), microcline (Mc), plagioclase (Pl), phyllosilicate (biotite, Bt), and intergranular and intragranular microcracks.

expansion coefficient of roughly 1.2×10^{-5}/°C (19–300°C; Heard & Page, 1982). The relative time shift due to thermal expansion is therefore likely small in comparison to our measurements (Figure 5b).

3.3. Acoustic Emission (AE) Monitoring

The total number of AE hits recorded during the first heating/cooling cycle (491) is greater than during the second (92) and third (46) cycles (Table 1). Figure 5c shows the number of AE hits against sample temperature in intervals of 10°C. We observed no significant variation in the amplitude or energy of AE hits during heating and cooling, and therefore, we report only the number of detected AE. The sample temperature was not recorded during the AE monitoring experiment to avoid noise from friction between the thermocouple and the sample. Instead, we calculate the sample temperature from the furnace temperature, and the sample and furnace temperatures measured during the CWI experiment. During the first heating cycle (Figure 5c), we begin to observe AE once the sample temperature exceeds 70°C, reaching a peak AE rate at 110°C. We see an increase in AE activity at around 250°C, and a second, larger increase between 310 and 450°C. During cooling, we record roughly the same number of AE hits as during heating (267 compared to 224; Table 1), and the AE rate is constant with temperature (Figure 5c). During the second cycle, the AE rate is lower overall than during the first cycle (Figure 5c) (with the exception of the larger number of hits as the sample reaches room temperature). During the third cycle, we record even fewer AE hits during both heating and cooling (Figure 5c).

4. Discussion

4.1. Thermal Microcracking

4.1.1. Onset of Thermal Microcracking

As we heat the Westerly Granite sample for the first time, we observe a slight increase in v_P and an increase in the CWI apparent velocity up until a sample temperature of roughly 60°C. From 70 °C we detect AE (Figure 5c) as a result of thermal microcracking, a threshold consistent with previous observations: 70–130°C in Westerly Granite (Bauer & Johnson, 1979; Hall & Bodnar, 1989; Johnson et al., 1978; Yong & Wang, 1980). The onset of AE marks the start of a significant decrease in v_P from 4.97 to 2.50 km/s at 450°C (Figure 5a), and an increase in the CWI relative time shift (Figure 5b). We continue to record AE throughout heating (Figure 5c), as previously observed in experiments on granite (Glover et al., 1995; Johnson et al., 1978), and we link the simultaneous velocity decrease and AE hits to the creation and propagation of thermal microcracks. Figure 6 shows SEM micrographs of an unheated sample of Westerly Granite, and a sample heated to and cooled from 450°C. Qualitatively, we observe more microcracks—both intragranular (through grains) and intergranular (along grain boundaries)—within the heated granite than within the unheated granite. We expect that in our case, thermal microcracking results from the build-up of mechanical stresses due to the differential thermal expansion of neighboring crystals rather than due to thermal gradients within the sample. Following the calculation of X.-Q. Wang et al. (2013), assuming a thermal diffusivity of granite of 10^{-6} m^2/s, the time constant for thermal equilibrium in our samples of radius 10 mm (the characteristic length) is 100 s. We assume that the thermal gradient within the sample is therefore negligible when heating and cooling at a rate of 1°C/min.

4.1.2. (Thermal) Kaiser Memory Effect

During cooling of the first cycle, we observe an increase in wave velocity (e.g., v_P increases from 2.5 to 3.0 km/s; Figures 5a and 5b), which we attribute to the closure of microcracks as crystals contract.

Following the first heating/cooling cycle, we heated the granite a second time (examples of repeated thermal stressing; e.g., Todd, 1973, and Yong and Wang, 1980, are rare in the literature). AE hits, observed from around 80°C, are far less frequent than during the first cycle (Table 1 and Figure 5c). From the beginning of heating we measure an immediate decrease in v_P, which continues throughout heating from 3.01 km/s at room temperature to 2.44 km/s at 450°C (Figure 5a) and, in the CWI measurements, a positive relative time shift (Figure 5b). This suggests that crystals are not as tightly interlocked as in the unheated granite and may expand owing to the presence of new microcracks along grain boundaries following the first cycle (Homand-Etienne & Houpert, 1989). During cooling of cycle two, v_P increases from 2.44 to 2.90 km/s (Figure 5a). The 0.11 km/s permanent decrease in velocity—also seen in our benchtop measurements of v_P at room temperature on another sample (Table 1)—is evidence of further microcracking (albeit much reduced) during the second cycle. Thermal microcracking during repeated heating cycles is in conflict with the Kaiser memory effect (Kaiser, 1953) whereby, to sustain damage, a material must be subject to stresses greater than those it has already experienced. The Kaiser memory effect has previously been observed during the thermal stressing of rock and concrete (Choi et al., 2005; Heap et al., 2013; Yong & Wang, 1980; Zuberek et al., 1998). We suggest that thermal microcrack formation during the second cycle may be due to remnant stresses within the granite following the first cycle. As the granite is heated for the third time, AE begins later still, at around 100°C, and we observe fewer AE than during the previous two cycles (Table 1 and Figure 5c). We measure a decrease in v_P from 2.90 to 2.42 km/s (Figure 5a) during heating and an increase from 2.42 to 2.85 km/s during cooling—0.05 km/s less than before heating. Again, these values are similar to our room temperature v_P measurements on another Westerly Granite sample (Table 1). During the third cycle, as the velocity change is almost entirely recovered, owing to the reversible opening and closing of microcracks, we expect very little thermal microcracking to have occurred. Thirumalai and Demou (1973), who performed thermal dilation measurements during repeated heating and cooling of granite, also observed no evolution in microcrack damage from the third thermal stressing cycle.

4.1.3. Thermal Microcracking During Cooling

During the first cycle, we detected a similar number of AE hits during cooling as during heating (Table 1). Browning et al. (2016), who heated two volcanic rocks (a basalt and a dacite) to 1100°C, found that the majority of the detected AE occurred during cooling, which they attributed to cooling-induced thermal microcracking. For Westerly Granite, the increase in v_P (from 2.50 km/s at 450°C to 3.01 km/s at room temperature; Figure 5a) and the CWI negative time shift (an increase in apparent velocity; Figure 5b) during cooling indicate that thermal microcracking is much less significant than during heating, despite the slightly greater number of AE hits detected during cooling (Table 1 and Figure 5c). However, we do still expect that some of the cooling AE is due to microcracking, as the velocity recovery during cooling is slightly less than during cycles 2 and 3, where velocity changes are near elastic (Figures 5a and 5b). Taken together, these observations suggest that although there was likely some thermal microcracking occurring during the cooling phase of cycle one, it is not easy to attribute the large number of recorded AE during cooling to microcracking. We therefore speculate that a large portion of the AE activity during the first cooling cycle was not associated with microcracking, but rather friction on microcrack surfaces as the crystals cool and contract. Although this is in conflict with the conclusion of Browning et al. (2016), we note that the process of thermal microcracking may differ between a crystalline rock (granite) and a volcanic rock that consists of phenocrysts within an amorphous groundmass.

4.2. v_P and v_S

Assuming that thermal microcracking in Westerly Granite is isotropic and homogeneous (Nasseri, Tatone, et al., 2009; and also shown to be the case in La Peyratte granite by C. David et al., 1999), and ignoring thermal strain effects, the relative time shift in the arrival times of scattered waves may be equated to a change in the velocity of the rock. We expect the coda to contain surface waves and multiple-reflected waves, which are both sensitive mostly to changes in v_S (Grêt et al., 2006; Snieder, 2002). First, the velocity of surface waves traveling around the sample is directly proportional to the shear wave velocity (typically 0.9 v_S). Second, as waves are scattered and reflected multiple times, they are converted from *P* to *S* waves, and vice versa. Snieder (2002) showed that once the *P* and *S* wave energies have reached equilibrium, the CWI apparent velocity change (provided by equation (1)) is more sensitive to changes in the velocity of *S* waves than *P* waves (equation (3) for a Poisson medium). For our CWI measurements, if we consider an *S* wave of

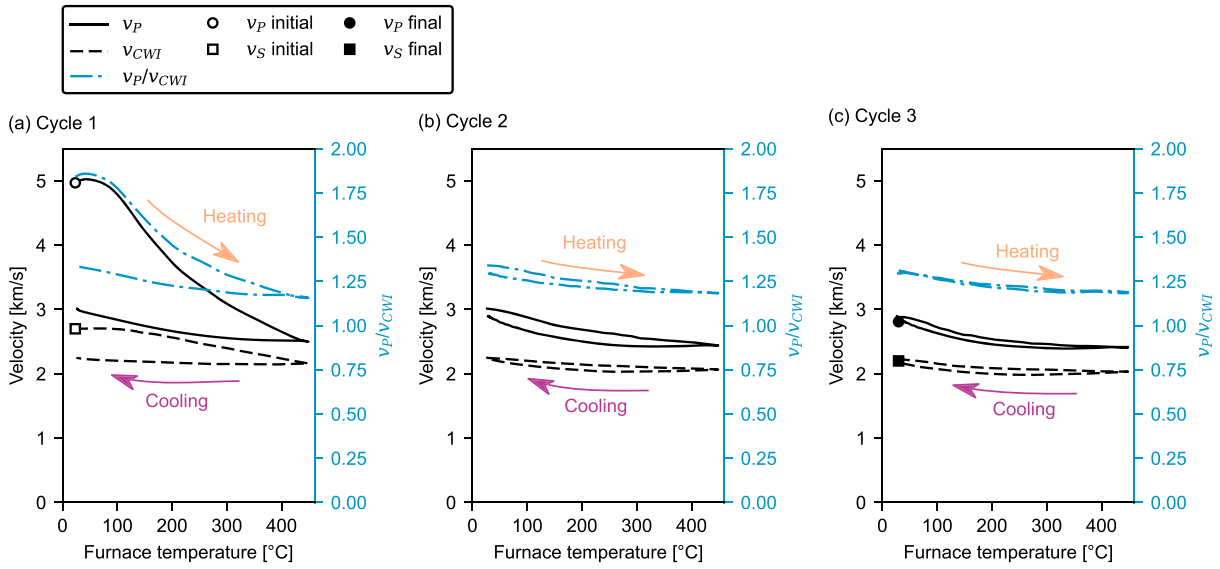

Figure 7. Wave velocity of Westerly Granite against sample temperature during (a–c) three heating and cooling cycles to a maximum temperature of 450°C. The symbols show static measurements of v_P (circles) and v_S (squares) made at room temperature using a separate device both before (open symbols) and following thermal stressing (closed symbols). The curves represent v_P (black solid), the CWI pseudo *S* wave velocity, v_{CWI}, (black dashed), and their ratio (blue dot-and-dashed). The v_P and v_{CWI} are calculated respectively from the time shift of the *P* wave first arrivals and the CWI relative time shift (equation (1)), scaled to the static v_P (4.97 km/s) and v_S (2.7 km/s) measurements of the unheated granite.

velocity 2.7 km/s (v_S of the unheated granite; Table 1), waves may travel a distance of up to 1.35 m, traversing the sample multiple times. We therefore assume that the *P* and *S* wave energies are equilibrated, which is the case following a few reflections/scatterings (Trégourès & van Tiggelen, 2002).

$$\frac{\delta v}{v} = 0.09\frac{\delta v_P}{v_P} + 0.91\frac{\delta v_S}{v_S} \tag{3}$$

Therefore, with CWI, the same waveform data used for our v_P measurements may inform on changes in v_S. Assuming that apparent changes in CWI velocity are equal to changes in v_S, in Figure 7, we calculate the pseudo *S* wave velocity, noted v_{CWI}, from the measurement of v_S at room temperature prior to heating, and the CWI relative time shift (similar to our approach for calculating v_P). Our room temperature measurements show a decrease in v_S from 2.7 km/s before heating to 2.2 km/s following all three heating/cooling cycles (Table 1). This is the same 17% decrease as observed by CWI (Figure 7) and is also compatible with the 15% permanent decrease in v_S measured by Nasseri, Schubnel, et al. (2009) when they heated Westerly Granite to 450°C (a single heating/cooling cycle).

Also in Figure 7, we show v_P and the ratio $\frac{v_P}{v_{CWI}}$, analogue to the $\frac{v_P}{v_S}$ ratio. The $\frac{v_P}{v_S}$ ratio is known to be sensitive to microcrack orientation and density (a function of the number and size of microcracks). In the case of isotropic thermal microcracking in dry granite, we expect $\frac{v_P}{v_S}$ to decrease with microcrack density (X.-Q. Wang et al., 2012). During the first cycle, we calculate a permanent decrease in $\frac{v_P}{v_{CWI}}$ from 1.84 to 1.34 (Figure 7) due to thermal microcracking. We note that a $\frac{v_P}{v_S}$ ratio of less than $\sqrt{2}\approx1.41$ results in a negative Poisson's ratio and, although theoretically plausible (Case, 1984; Walsh, 1965), is rare among isotropic materials. Homand-Etienne and Houpert (1989) also found a negative Poisson's ratio for two thermally microcracked granites (Senones Granite and Remiremont Granite heated to 200–600°C); they suggested that residual stresses during cooling are the cause of this unexpected mechanical behavior.

During cycles 2 and 3, we observe a near reversible decrease in $\frac{v_P}{v_{CWI}}$ with increasing temperature (Figure 7). We expect that the evolution of $\frac{v_P}{v_{CWI}}$ with temperature during the second and third cycles is due to the thermo-elastic deformation of crystals. The decrease in $\frac{v_P}{v_{CWI}}$ with temperature could be due to a widening of preexisting microcracks as crystals expand: assuming that cracks are dry and elliptical, an increase in crack aspect ratio corresponds to an increase in crack density and, in turn, a decrease in $\frac{v_P}{v_S}$ ratio (O'Connell &

Budiansky, 1974). A dedicated study would be needed to further assess the influence of temperature on the elastic moduli of Westerly Granite.

4.3. Geothermal Implications

Thermal microcracking in granite is known to lower stiffness and strength (Wong, 1982), lower thermal diffusivity (Heuze, 1983; Kant et al., 2017), and increase permeability (Darot et al., 1992; C. David et al., 1999; Heard & Page, 1982; Nasseri, Schubnel, et al., 2009; Violay et al., 2017): all parameters that can influence the exploitation and modeling of geothermal resources. Granite is the reservoir rock for the many geothermal projects in the Upper Rhine Graben, including those at Soultz-sous-Forêts (France) (e.g., A. Gérard & Kappelmeyer, 1987; André Gérard et al., 2006) and Rittershoffen (France) (e.g., Baujard et al., 2017). In such a thermally dynamic environment, it is important to consider the evolution of the intrinsic mechanical and transport properties of rock with temperature. Our velocity measurements of granite are strongly dependent on temperature—due to the thermal expansion and contraction of crystals and the formation and propagation of thermal microcracks—and highlight the importance of performing measurements under in situ temperature conditions. Potential differences in rock properties with temperature should be understood when applying laboratory measurements made under ambient conditions to the modeling of and monitoring of geothermal systems.

While our results exhibit (to a degree) a Kaiser memory effect—whereby repeated thermal stressing does not further induce thermal microcracking (Figure 5)—reservoir conditions may favor repeated thermal microcracking, over longer durations. First, thermal stresses further accumulate over time and space in a geothermal reservoir, as fluid penetrates deeper into the rock mass through the newly created crack porosity (Dempsey et al., 2015; Murphy, 1978). Thermal stresses may also contribute to stress-induced subcritical crack growth within the reservoir and around the borehole, leading to damage accumulation over time (Bérard & Cornet, 2003). Finally, our short-term (and dry) experiments do not allow for crack sealing due to hydrothermal precipitation, which is known to occur in geothermal reservoirs (Batzle & Simmons, 1976; Griffiths et al., 2016). Crack sealing increases rock cohesion and strength, allowing cracks to recrack (Engelder, 1987)—a phenomenon which has been reproduced in the laboratory (Karner et al., 1997). In a geothermal environment, thermal stresses may therefore play an important role in the evolution of crack damage over time.

Our velocity measurements are also relevant for geothermal reservoir monitoring. During the hydraulic stimulation (through water injection) of the Soultz-sous–Forêts geothermal reservoir, earthquake tomography inversions revealed changes in v_P, which coincided with changes in the injection flow rate (Calò et al., 2011). From our results, we speculate that a significant portion of velocity changes may be a consequence of temperature changes due to the circulating fluids. CWI, through correlation of ambient seismic noise, has been used to link velocity changes to geothermal reservoir activities (Lehujeur et al., 2017; Obermann et al., 2015). At a geothermal reservoir, v_P, v_S, and their ratio are often interpreted in terms of fluid saturation; however, our results suggest that temperature effect of circulating fluids may also play a significant role. Note that at the scale of the geothermal reservoir, the wave velocity of rock may be lower than velocities measured in the laboratory due to the lower frequency of seismic waves compared to ultrasonic waves (Zoback, 2010). Further, within a geothermal reservoir, changes in temperature and related changes in velocity are localized, whereas here the temperature varied throughout the sample. At the reservoir scale there will be a limit in the resolution of seismic tomography depending on the amplitude of the localized velocity changes and the affected volume.

We chose to perform these measurements on the well-studied Westerly Granite; however, many geothermal reservoirs are hosted in volcanic rock (Grant, 2013), and we may expect differences in the mechanisms for thermal microcracking in such rock due to differences in microstructure and porosity. For example, there is evidence to suggest that thermal microcracking in volcanic rocks occurs primarily during cooling (Browning et al., 2016), and volcanic rocks with a high preexisting crack density prior to heating are thought to exhibit less thermal microcracking during heating/cooling (Heap et al., 2014; Vinciguerra et al., 2005). The influence of temperature on thermal microcracking and velocity in different rock types merits further study.

Through our experiments, in which we heated granite samples from ambient temperature, we offer insight into the potential for thermal microcracking in a geothermal environment. However, thermal microcracking may also be induced by the quenching of hot rock by cooler fluids (Siratovich et al., 2015). For example, the

use of cool drilling fluid in geothermal wells has been shown to induce borehole breakouts (Bérard & Cornet, 2003), and the injection of cool water has even been actively used to enhance permeability within the reservoir, in a technique known as thermal stimulation (Grant et al., 2013; Jeanne et al., 2017; Kitao et al., 1995). Further research into the particularity of cooling-induced cracking would complement our study.

A final research perspective is the influence of confining pressure on thermal microcracking and ultrasonic velocity. At the Soultz-sous-Forêts geothermal site, for example, the pressure increase in the vertical stress component increases by around 25 MPa per kilometer depth, and the horizontal components are of a similar order of magnitude (Cornet & Bérard, 2003; Genter et al., 2010; Valley & Evans, 2007). During heating, thermal microcracking may be inhibited by high confining pressures (Siddiqi & Evans, 2015; Van der Molen, 1981; Wong & Brace, 1979) and, at room temperature, the v_P and v_S of thermally microcracked Westerly Granite have been shown to increase with confining pressure (Nasseri, Schubnel, et al., 2009). H. F. Wang et al. (1989) measured v_P of Westerly Granite during heating to and cooling from 300°C, under confining pressures of 7, 28, and 55 MPa. H. F. Wang et al. (1989) found that for all confining pressures, v_P decreased during heating and increased during cooling, back to the velocity of the unheated rock. For example, under 7 MPa confining pressure, v_P decreased from ~4.5 km/s at room temperature to ~3.4 km/s at 300°C and increased back to ~4.5 km/s during cooling. Violay et al. (2017) performed high-temperature (up to 1000°C), high-pressure (130 MPa) triaxial experiments on Westerly Granite samples to emulate conditions within the ductile crust. Violay et al. (2017) found that when samples were heated to the target temperatures under a confining pressure, their permeabilities (at pressure and temperature) were higher when the temperature was higher, interpreted by these authors as a result of thermal microcracking. The results of Violay et al. (2017) and H. F. Wang et al. (1989) show that thermal microcracks in granite may open (and remain open) when heated under confining pressure. Further experiments are now required to better understand thermal microcracking under a confining pressure.

5. Conclusions

Through the combined use of AE monitoring and in situ v_P and CWI measurements, we observed both permanent (microcracking) and nonpermanent (crack opening and closing) changes in the microstructure of Westerly Granite when repeatedly heated and cooled, at ambient pressure, to a maximum temperature of 450°C. Following a slight initial increase in velocity with temperature during heating, from the onset of AE at around 70°C, we observed a large—and mostly permanent—reduction in velocity with temperature due to thermal microcracking. Thermal microcracking is a result of the build-up of mechanical stresses due to the mismatch in thermal expansion of crystals. During cooling we detected AE (slightly more than during heating) but the measured increase in velocity suggests that the source of AE cannot be entirely attributed to thermal microcracking: AE may instead be due to friction on microcrack surfaces as crystals cool and contract. We observed some, but less microcracking during the second cycle, and less again during the third cycle. During these two cycles, the reversible change in velocity with heating and cooling is nonnegligible: v_P decreased by roughly 10% of the initial velocity when heated to 450°C. We attribute the reversible increase/decrease in velocity to the elastic expansion/contraction of crystals, and the associated opening/closing of microcracks. We show how CWI can be used to monitor microcracking at high temperature and, in the case of isotropic and homogeneous microcracking, provide a measure of v_S. Our velocity measurements made during the thermal stressing of Westerly Granite—which add to existing measurements in the literature made on thermally-stressed rock under ambient conditions—highlight the value of performing measurements of rock properties under in situ temperature conditions, to provide more relevant data for seismic and geomechanical modeling.

Acknowledgments
This work has been published under the framework of LABEX grant ANR-11-LABX-0050_G-EAU-THERMIE-PROFONDE and therefore benefits from state funding managed by the Agence Nationale de la Recherche (ANR) as part of the "Investissements d'avenir" program. We also acknowledge ANR grant CANTARE (ANR-15-CE06-0014-01). The authors would like to thank Bertrand Renaudié for sample preparation and Alexandre Schubnel for kindly furnishing the block of Westerly Granite (with the help of Lucas Pimienta), and Alain Steyer and Laurent Rihouey for their help with the construction of the experimental setup. The DOI of the data presented here is 10.6084/m9.figshare.5900875.

References

Batzle, M. L., & Simmons, G. (1976). Microfractures in rocks from two geothermal areas. *Earth and Planetary Science Letters*, *30*(1), 71–93. https://doi.org/10.1016/0012-821X(76)90010-8

Bauer, S. J., & Johnson, B. (1979). Effects of slow uniform heating on the physical properties of the Westerly and Charcoal granites. In 20th US Symposium on Rock Mechanics (USRMS). American Rock Mechanics Association. Retrieved from https://www.onepetro.org/conference-paper/ARMA-79-0007

Baujard, C., Genter, A., Dalmais, E., Maurer, V., Hehn, R., Rosillette, R., et al. (2017). Hydrothermal characterization of wells GRT-1 and GRT-2 in Rittershoffen, France: Implications on the understanding of natural flow systems in the rhine graben. *Geothermics*, *65*, 255–268.

Bérard, T., & Cornet, F. H. (2003). Evidence of thermally induced borehole elongation: A case study at Soultz, France. *International Journal of Rock Mechanics and Mining Sciences*, *40*(7–8), 1121–1140. https://doi.org/10.1016/S1365-1609(03)00118-7

Browning, J., Meredith, P., & Gudmundsson, A. (2016). Cooling-dominated cracking in thermally stressed volcanic rocks. *Geophysical Research Letters*, *43*, 8417–8425. https://doi.org/10.1002/2016GL070532

Calò, M., Dorbath, C., Cornet, F. H., & Cuenot, N. (2011). Large-scale aseismic motion identified through 4-D P-wave tomography: Temporal subsetting of the stimulation period. *Geophysical Journal International*, *186*(3), 1295–1314. https://doi.org/10.1111/j.1365-246X.2011.05108.x

Case, E. D. (1984). The effect of microcracking upon the Poisson's ratio for brittle materials. *Journal of Materials Science*, *19*(11), 3702–3712.

Chaki, S., Takarli, M., & Agbodjan, W. P. (2008). Influence of thermal damage on physical properties of a granite rock: Porosity, permeability and ultrasonic wave evolutions. *Construction and Building Materials*, *22*(7), 1456–1461. https://doi.org/10.1016/j.conbuildmat.2007.04.002

Chen, S., Yang, C., & Wang, G. (2017). Evolution of thermal damage and permeability of Beishan granite. *Applied Thermal Engineering*, *110*, 1533–1542. https://doi.org/10.1016/j.applthermaleng.2016.09.075

Choi, N.-S., Kim, T.-W., & Rhee, K. Y. (2005). Kaiser effects in acoustic emission from composites during thermal cyclic-loading. *NDT and E International*, *38*(4), 268–274. https://doi.org/10.1016/j.ndteint.2004.09.005

Cornet, F. H., & Bérard, T. (2003). A case example of integrated stress profile evaluation. In K. Sugawara, Y. Obara, & A. Sato (Eds.), *3rd International Symposium on Rock Stress* (pp. 23–24).

Darot, M., Gueguen, Y., & Baratin, M.-L. (1992). Permeability of thermally cracked granite. *Geophysical Research Letters*, *19*, 869–872. https://doi.org/10.1029/92GL00579

David, C., Menendez, B., & Darot, M. (1999). Influence of stress-induced and thermal cracking on physical properties and microstructure of La Peyratte granite. *International Journal of Rock Mechanics and Mining Sciences*, *36*(4), 433–448.

David, E. C., Brantut, N., Schubnel, A., & Zimmerman, R. W. (2012). Sliding crack model for nonlinearity and hysteresis in the uniaxial stress-strain curve of rock. *International Journal of Rock Mechanics and Mining Sciences*, *52*, 9–17. https://doi.org/10.1016/j.ijrmms.2012.02.001

Dempsey, D., Kelkar, S., Davatzes, N., Hickman, S., & Moos, D. (2015). Numerical modeling of injection, stress and permeability enhancement during shear stimulation at the Desert Peak Enhanced Geothermal System. *International Journal of Rock Mechanics and Mining Sciences*, *78*, 190–206. https://doi.org/10.1016/j.ijrmms.2015.06.003

Engelder, T. (1987). Joints and shear fractures in rock. In *Fracture Mechanics of Rock* (pp. 27–69). Orlando, FL: Academic Press.

Fredrich, J. T., & Wong, T. (1986). Micromechanics of thermally induced cracking in three crustal rocks. *Journal of Geophysical Research*, *91*, 12,743–12,743. https://doi.org/10.1029/JB091iB12p12743

Fukuhara, M., & Sanpei, A. (1994). High temperature-elastic moduli and internal dilational and shear frictions of fused quartz. *Japanese Journal of Applied Physics*, *33*, 2890–2893. https://doi.org/10.1143/JJAP.33.2890

Genter, A., Evans, K., Cuenot, N., Fritsch, D., & Sanjuan, B. (2010). Contribution of the exploration of deep crystalline fractured reservoir of Soultz to the knowledge of enhanced geothermal systems (EGS). *Comptes Rendus Geoscience*, *342*(7–8), 502–516. https://doi.org/10.1016/j.crte.2010.01.006

Gérard, A., Genter, A., Kohl, T., Lutz, P., Rose, P., & Rummel, F. (2006). The deep EGS (Enhanced Geothermal System) project at Soultz-sous-Forêts (Alsace, France). *Geothermics*, *35*(5–6), 473–483. https://doi.org/10.1016/j.geothermics.2006.12.001

Gérard, A., & Kappelmeyer, O. (1987). The Soultz-sous-Forêts project. *Geothermics*, *16*(4), 393–399.

Glover, P. W. J., Baud, P., Darot, M., Meredith, P. G., Boon, S. A., LeRavalec, M., et al. (1995). Alpha/Beta phase transitions in quartz monitored using acoustic emissions. *Geophysical Journal International*, *120*, 775–782.

Grant, M. A. (2013). *Geothermal reservoir engineering*. Elsevier.

Grant, M. A., Clearwater, J., Quinao, J., Bixley, P. F., & Le Brun, M. (2013). Thermal stimulation of geothermal wells: A review of field data. Thirty-Eighth Workshop on Geothermal Reservoir Engineering, Stanford University, Stanford, California, February 11–13, 2013.

Grêt, A., Snieder, R., & Scales, J. (2006). Time-lapse monitoring of rock properties with coda wave interferometry. *Journal of Geophysical Research*, *111*, B03305. https://doi.org/10.1029/2004JB003354

Griffiths, L., Heap, M. J., Wang, F., Daval, D., Gilg, H. A., Baud, P., et al. (2016). Geothermal implications for fracture-filling hydrothermal precipitation. *Geothermics*, *64*, 235–245. https://doi.org/10.1016/j.geothermics.2016.06.006

Hall, D. L., & Bodnar, R. J. (1989). Comparison of fluid inclusion decrepitation and acoustic emission profiles of Westerly granite and Sioux quartzite. *Tectonophysics*, *168*(4), 283–296. https://doi.org/10.1016/0040-1951(89)90223-0

Heap, M. J., Lavallée, Y., Laumann, A., Hess, K. U., Meredith, P. G., Dingwell, D. B., et al. (2013). The influence of thermal-stressing (up to 1000°C) on the physical, mechanical, and chemical properties of siliceous-aggregate, high-strength concrete. *Construction and Building Materials*, *42*, 248–265. https://doi.org/10.1016/j.conbuildmat.2013.01.020

Heap, M. J., Lavallée, Y., Petrakova, L., Baud, P., Reuschlé, T., Varley, N. R., & Dingwell, D. B. (2014). Microstructural controls on the physical and mechanical properties of edifice-forming andesites at Volcán de Colima, Mexico. *Journal of Geophysical Research: Solid Earth*, *119*, 2925–2963. https://doi.org/10.1002/2013JB010521

Heard, H. C., & Page, L. (1982). Elastic moduli, thermal expansion, and inferred permeability of two granites to 350°C and 55 megapascals. *Journal of Geophysical Research*, *87*, 9340–9340. https://doi.org/10.1029/JB087iB11p09340

Heuze, F. E. (1983). High-temperature mechanical, physical and Thermal properties of granitic rocks—A review. *International Journal of Rock Mechanics and Mining Science and Geomechanics Abstracts*, *20*(1), 3–10. https://doi.org/10.1016/0148-9062(83)91609-1

Homand-Etienne, F., & Houpert, R. (1989). Thermally induced microcracking in granites: characterization and analysis. *International Journal of Rock Mechanics and Mining Science and Geomechanics Abstracts*, *26*(2), 125–134. https://doi.org/10.1016/0148-9062(89)90001-6

Jeanne, P., Rutqvist, J., & Dobson, P. F. (2017). Influence of injection-induced cooling on deviatoric stress and shear reactivation of preexisting fractures in Enhanced Geothermal Systems. *Geothermics*, *70*, 367–375. https://doi.org/10.1016/j.geothermics.2017.08.003

Johnson, B., Gangi, A. F., Handin, J. (1978). Thermal cracking of rock subjected to slow, uniform temperature changes. In 19th US Symposium on Rock Mechanics (USRMS). American Rock Mechanics Association.

Jones, C., Keaney, G., Meredith, P., & Murrell, S. (1997). Acoustic emission and fluid permeability measurements on thermally cracked rocks. *Physics and Chemistry of the Earth*, *22*(1), 13–17. https://doi.org/10.1016/S0079-1946(97)00071-2

Kaiser, J. (1953). Erkenntnisse und Folgerungen aus der Messung von Geräuschen bei Zugbeanspruchung von metallischen Werkstoffen. *Archiv für das Eisenhüttenwesen*, *24*(1–2), 43–45. https://doi.org/10.1002/srin.195301381

Kant, M. A., Ammann, J., Rossi, E., Madonna, C., Höser, D., & von Rohr, P. R. (2017). Thermal properties of Central Aare granite for temperatures up to 500°C: irreversible changes due to thermal crack formation. *Geophysical Research Letters*, *44*, 771–776. https://doi.org/10.1002/2016GL070990

Karner, S. L., Marone, C., & Evans, B. (1997). Laboratory study of fault healing and lithification in simulated fault gouge under hydrothermal conditions. *Tectonophysics*, *277*(1), 41–55. https://doi.org/10.1016/S0040-1951(97)00077-2

Kern, H. (1982). Elastic-wave velocity in crustal and mantle rocks at high pressure and temperature: the role of the high-low quartz transition and of dehydration reactions. *Physics of the Earth and Planetary Interiors*, *29*(1), 12–23.
Kitao, K., Ariki, K., Watanabe, H., & Wakita, K. (1995). Cold-water well stimulation experiments in the Sumikawa geothermal field, Japan. *Bulletin of the Geothermal Resources Council*, *24*(2), 53–61.
Kranz, R. L. (1983). Microcracks in rocks: A review. *Tectonophysics*, *100*(1–3), 449–480.
Larose, E., & Hall, S. (2009). Monitoring stress related velocity variation in concrete with a 2$\times$ 10–5 relative resolution using diffuse ultrasound. *The Journal of the Acoustical Society of America*, *125*(4), 1853–1856.
Lehujeur, M., Vergne, J., Maggi, A., & Schmittbuhl, J. (2017). Ambient noise tomography with non-uniform noise sources and low aperture networks: Case study of deep geothermal reservoirs in northern Alsace, France. *Geophysical Journal International*, *208*(1), 193–210. https://doi.org/10.1093/gji/ggw373
Lockner, D. A. (1998). A generalized law for brittle deformation of Westerly granite. *Journal of Geophysical Research*, *103*, 5107–5123. https://doi.org/10.1029/97JB03211
Meredith, P. G., & Atkinson, B. K. (1985). Fracture toughness and subcritical crack growth during high-temperature tensile deformation of Westerly granite and Black gabbro. *Physics of the Earth and Planetary Interiors*, *39*(1), 33–51. https://doi.org/10.1016/0031-9201(85)90113-X
Meredith, P. G., Main, I. G., Clint, O. C., & Li, L. (2012). On the threshold of flow in a tight natural rock. *Geophysical Research Letters*, *39*, L04307. https://doi.org/10.1029/2011GL050649
Murphy, H. D. (1978). *Thermal stress cracking and the enhancement of heat extraction from fractured geothermal reservoirs*. New Mexico: Los Alamos Scientific Lab.
Nasseri, M. H. B., Schubnel, A., Benson, P. M., & Young, R. P. (2009). Common evolution of mechanical and transport properties in thermally cracked Westerly Granite at elevated hydrostatic pressure. *Pure and Applied Geophysics*, *166*(5–7), 927–948. https://doi.org/10.1007/s00024-009-0485-2
Nasseri, M. H. B., Schubnel, A., & Young, R. P. (2007). Coupled evolutions of fracture toughness and elastic wave velocities at high crack density in thermally treated Westerly granite. *International Journal of Rock Mechanics and Mining Sciences*, *44*(4), 601–616. https://doi.org/10.1016/j.ijrmms.2006.09.008
Nasseri, M. H. B., Tatone, B. S. A., Grasselli, G., & Young, R. P. (2009). Fracture toughness and fracture roughness interrelationship in thermally treated westerly granite. In *Rock Physics and Natural Hazards* (pp. 801–822). Basel: Birkhäuser. https://doi.org/10.1007/978-3-0346-0122-1_4
Obermann, A., Kraft, T., Larose, E., & Wiemer, S. (2015). Potential of ambient seismic noise techniques to monitor the St. Gallen geothermal site (Switzerland): Monitoring the St. Gallen Geothermal Site. *Journal of Geophysical Research: Solid Earth*, *120*, 4301–4316. https://doi.org/10.1002/2014JB011817
O'Connell, R. J., & Budiansky, B. (1974). Seismic velocities in dry and saturated cracked solids. *Journal of Geophysical Research*, *79*, 5412–5426. https://doi.org/10.1029/JB079i035p05412
Poupinet, G., Ellsworth, W. L., & Frechet, J. (1984). Monitoring velocity variations in the crust using earthquake doublets: An application to the Calaveras Fault, California. *Journal of Geophysical Research*, *89*, 5719–5731. https://doi.org/10.1029/JB089iB07p05719
Reuschlé, T., Gbaguidi Haore, S., & Darot, M. (2003). Microstructural control on the elastic properties of thermally cracked granite. *Tectonophysics*, *370*(1–4), 95–104. https://doi.org/10.1016/S0040-1951(03)00179-3
Sens-Schönfelder, C., & Wegler, U. (2006). Passive image interferometry and seasonal variations of seismic velocities at Merapi Volcano, Indonesia. *Geophysical Research Letters*, *33*, L21302. https://doi.org/10.1029/2006GL027797
Siddiqi, G., & Evans, B. (2015). Permeability and thermal cracking at pressure in Sioux Quartzite. *Geological Society, London, Special Publications*, *409*(1), 49–66.
Siratovich, P. A., Villeneuve, M. C., Cole, J. W., Kennedy, B. M., & Bégué, F. (2015). Saturated heating and quenching of three crustal rocks and implications for thermal stimulation of permeability in geothermal reservoirs. *International Journal of Rock Mechanics and Mining Sciences*, *80*, 265–280. https://doi.org/10.1016/j.ijrmms.2015.09.023
Snieder, R. (2002). Coda wave interferometry and the equilibration of energy in elastic media. *Physical Review E*, *66*(4). https://doi.org/10.1103/PhysRevE.66.046615
Snieder, R. (2006). The theory of coda wave interferometry. *Pure and Applied Geophysics*, *163*(2–3), 455–473. https://doi.org/10.1007/s00024-005-0026-6
Snieder, R., Grêt, A., Douma, H., & Scales, J. (2002). Coda wave interferometry for estimating nonlinear behavior in seismic velocity. *Science*, *295*(5563), 2253–2255.
Thirumalai, K., & Demou, S. (1973). *Thermal expansion behaviour of intact and thermal fractured mine rocks*. Paper presented at 19th Annual American Institute of Physics Conference, Boston, MA.
Todd, T. P. (1973). *Effect of cracks on elastic properties of low porosity rocks* (PhD thesis). Massachusetts Institute of Technology, Cambridge.
Trégourès, N. P., & van Tiggelen, B. A. (2002). Quasi-two-dimensional transfer of elastic waves. *Physical Review E*, *66*(3). https://doi.org/10.1103/PhysRevE.66.036601
Valley, B., & Evans, K. F. (2007). Stress state at Soultz-sous-Forêts to 5 km depth from wellbore failure and hydraulic observations. In *Proceedings, 32nd workshop on geothermal reservoir engineering* (pp. 17,481–17,469).
Van der Molen, I. (1981). The shift of the α-β transition temperature of quartz associated with the thermal expansion of granite at high pressure. *Tectonophysics*, *73*(4), 323–342. https://doi.org/10.1016/0040-1951(81)90221-3
Vinciguerra, S., Trovato, C., Meredith, P. G., & Benson, P. M. (2005). Relating seismic velocities, thermal cracking and permeability in Mt. Etna and Iceland basalts. *International Journal of Rock Mechanics and Mining Sciences*, *42*, 900–910. https://doi.org/10.1016/j.ijrmms.2005.05.022
Violay, M., Heap, M. J., Acosta, M., & Madonna, C. (2017). Porosity evolution at the brittle-ductile transition in the continental crust: Implications for deep hydro-geothermal circulation. *Scientific Reports*, *7*. https://doi.org/10.1038/s41598-017-08108-5
Walsh, J. B. (1965). The effect of cracks in rocks on Poisson's ratio. *Journal of Geophysical Research*, *70*, 5249–5257. https://doi.org/10.1029/JZ070i020p05249
Wang, H. F., Bonner, B. P., Carlson, S. R., Kowallis, B. J., & Heard, H. C. (1989). Thermal stress cracking in granite. *Journal of Geophysical Research*, *94*, 1745–1758. https://doi.org/10.1029/JB094iB02p01745
Wang, X.-Q., Schubnel, A., Fortin, J., David, E. C., Guéguen, Y., & Ge, H.-K. (2012). High Vp/Vs ratio: Saturated cracks or anisotropy effects? *Geophysical Research Letters*, *39*, L11307. https://doi.org/10.1029/2012GL051742
Wang, X.-Q., Schubnel, A., Fortin, J., Guéguen, Y., & Ge, H.-K. (2013). Physical properties and brittle strength of thermally cracked granite under confinement. *Journal of Geophysical Research: Solid Earth*, *118*, 6099–6112. https://doi.org/10.1002/2013JB010340

Wong, T. -f. (1982). Micromechanics of faulting in westerly granite. *International Journal of Rock Mechanics and Mining Science and Geomechanics Abstracts*, *19*(2), 49–64. https://doi.org/10.1016/0148-9062(82)91631-X

Wong, T.-f., & Brace, W. F. (1979). Thermal expansion of rocks: some measurements at high pressure. *Tectonophysics*, *57*(2), 95–117. https://doi.org/10.1016/0040-1951(79)90143-4

Yong, C., & Wang, C. (1980). Thermally induced acoustic emission in Westerly granite. *Geophysical Research Letters*, *7*, 1089–1092.

Zappone, A. S., & Benson, P. M. (2013). Effect of phase transitions on seismic properties of metapelites: A new high-temperature laboratory calibration. *Geology*, *41*(4), 463–466. https://doi.org/10.1130/G33713.1

Zhang, Y., Abraham, O., Tournat, V., Le Duff, A., Lascoup, B., Loukili, A., et al. (2013). Validation of a thermal bias control technique for Coda Wave Interferometry (CWI). *Ultrasonics*, *53*(3), 658–664. https://doi.org/10.1016/j.ultras.2012.08.003

Zoback, M. D. (2010). *Reservoir geomechanics*. Cambridge University Press.

Zuberek, W. M., Zogała, B., Dubiel, R., & Pierwoła, J. (1998). Maximum temperature memory in sandstone and mudstone observed with acoustic emission and ultrasonic measurements. *International Journal of Rock Mechanics and Mining Sciences*, *35*(4–5), 416–417. https://doi.org/10.1016/S0148-9062(98)00115-6